

Journal of Materials Chemistry A

Accepted Manuscript



This is an *Accepted Manuscript*, which has been through the Royal Society of Chemistry peer review process and has been accepted for publication.

Accepted Manuscripts are published online shortly after acceptance, before technical editing, formatting and proof reading. Using this free service, authors can make their results available to the community, in citable form, before we publish the edited article. We will replace this *Accepted Manuscript* with the edited and formatted *Advance Article* as soon as it is available.

You can find more information about *Accepted Manuscripts* in the [Information for Authors](#).

Please note that technical editing may introduce minor changes to the text and/or graphics, which may alter content. The journal's standard [Terms & Conditions](#) and the [Ethical guidelines](#) still apply. In no event shall the Royal Society of Chemistry be held responsible for any errors or omissions in this *Accepted Manuscript* or any consequences arising from the use of any information it contains.

Vertically Aligned VO₂(B) Nanobelt Forest and Its Three-Dimensional Structure on Oriented Graphene for Energy Storage

Guofeng Ren¹, Md Nadim Ferdous Hoque¹, Xuan Pan^{1†}, Juliusz Warzywoda², and Zhaoyang Fan^{1*}

¹Department of Electrical and Computer Engineering and Nano Tech Center, Texas Tech University, Lubbock, Texas, 79409, USA;

²Materials Characterization Center, Whitacre College of Engineering, Texas Tech University, Lubbock, Texas 79409, USA.

[†] Present address: Wuhan Branch of the National Science Library, Chinese Academy of Sciences, Wuhan 430071, China.

* Corresponding author: zhaoyang.fan@ttu.edu

Abstract

Assembling two-dimensional (2D) nanomaterials into an ordered forest structure that provides easily accessible large surface area and/or chemically active 2D edges, will present numerous opportunities, including as electrodes for energy storage. We report densely-packed vertically-aligned VO₂(B) nanobelts (NBs) based forest structure synthesized by solvothermal method using vertically-oriented graphene (VOG) network as the underlying support. We further expanded this forest structure into a folded three-dimensional (3D) forest structure using VOG-covered metallic foam as scaffold. To demonstrate its potential, this free-standing 3D ordered

structure built from 2D nanomaterial was directly used as electrode for lithium-ion batteries. Excellent performance was confirmed with a stable discharge capacity of 178 mAh g⁻¹ at a current density of 10 A g⁻¹ (or a rate of 59 C) and 100 mAh g⁻¹ at 27 A g⁻¹ (300 C), contributed by both lithium ion intercalation into the crystal lattice and surface-determined pseudocapacitance. A high cycling stability over 2,000 cycles under a high current density was also demonstrated. We expect that our method can be expanded to synthesize 2D sheets based forest structures of other layered oxides and hydroxides by using VOG as a versatile platform for numerous applications such as energy storage and catalytic energy conversion.

1. Introductions

2D layered materials are at the emerging frontiers of research and development.¹⁻⁶ The application of these 2D nanosheets (NSs), leveraging their novel properties, is highly anticipated. A grand challenge for assembling 2D NSs into 3D macrostructures for many crucial applications in general, and for battery electrode in particular, is how to densely pack NSs with enough active mass, maintain their 2D characteristics, provide an ordered porous geometry, offer electronic conductive paths, and simultaneously achieve mechanical robustness. Efforts to generate 2D NSs that are vertically oriented on a substrate to form maze-like networks or nanowall structures represent a step in this direction by providing a structure with easily accessible large surface area and/or their active edges. This is in contrast to the random clusters, which are formed from 2D NSs colloids or suspensions. The

vertically oriented NSs networks have been well documented for several transition metal oxides and hydroxides.⁷⁻¹² However, most of these vertical networks have a very limited height. Therefore, the effective mass loading in the structure is considerably low, significantly restricting their practical applications when considering their functionality in terms of per unit cross-sectional area, unit volume, or unit mass of the whole structure.

Recently, accompanied by intense efforts to develop nanostructured electrodes¹³⁻¹⁸ for electrochemical energy storage and energy conversion, nickel or graphene foams used as a 3D scaffold to support nanomaterials, including 2D NSs, have attracted considerable interest.¹⁹⁻²² Self-assembling 2D NSs orthogonally around a 3D conductive scaffold represents controlled manufacturing of 2D material into a 3D macrostructure, enabling a variety of applications that include high-performance electrochemical energy storage. Such nanostructured electrodes may address the interrelated issues of energy density, power density, charge-discharge rate, and cycling stability of electrochemical energy storage devices, especially lithium ion batteries (LIBs).^{23, 24} However, considering that the conductive foam generally has void space in the range of 10-100 μm , the commonly reported sub-micrometer height of orthogonally oriented 2D NSs again becomes an insurmountable obstacle when considering per unit volume or mass functionality of the whole structure. In addition to metal foams, branched nanosheets radially grown around nanowires or nanotubes,^{25, 26} and flower-like nanobelt or nanoflake clusters^{27, 28} are other examples of controlled

assembling of 2D materials. But again, these nanosheets or nanobelts have limited length.

New approaches to obtain densely-packed vertical, or more generally orthogonal, NSs with large height are therefore highly desirable. In contrast to 2D NSs, one-dimensional (1D) nanomaterials have been extensively reported to form densely-packed and vertically-aligned array (or forest) structures with height of tens of micrometers or larger. Downscaling the footprint, or the width, of vertical NSs might be effective in promoting densified nucleation and elongated height, a geometry of nanobelt (NB). NB-based array structures,^{29, 30} produced by chemical vapor deposition (CVD) process with each NB having a width of tens of nanometers, have been reported under the category of 1D nanomaterials since the width dimension is comparable with the diameter of nanowires and in the range of quantum confinement. However, if NBs have a width on the order of hundreds of nanometers or larger, they should be counted as 2D materials, considering that at such a scale, there will be no quantum confinement along the width direction.

To achieve the goal of densely packing vertical or orthogonal 2D nanomaterials with large height for sufficient mass loading, we selected layered VO₂(B) as a model 2D material. Different VO₂(B) nanostructures, especially in the context of energy storage, have been extensively reported. These structures include nanoscroll,³¹ nanothorn- or nanowire-based hollow microsphere,³²⁻³⁴ nanosheet-based 3D flower,²⁷ nanobelt,^{35, 36} ribbon,³⁷ and others. However, it is worth to emphasize that the reported VO₂(B) NBs and/or ribbons, used either as pure VO₂(B)³⁸ or as

composite in combination with carbon,³⁵ carbon nanotube,³⁶ or graphene,³⁷ were formed as precipitates or suspensions, and they were not vertically aligned forest structures. Here, we report VO₂(B) NBs-based forest structures with NBs having a width of up to 1-2 μm, a height up to more than 20 μm, and belt thickness ranging from tens down to a few nanometers. Such a forest structure was further grown inside of a compressed foam with orthogonally aligned VO₂(B) NBs encircling/surrounding the underlying conductive struts in radial direction to construct a 3D interconnected electrodes. Such a structure, with active 2D NBs closely packed into the void spacing of the foam in an ordered arrangement, moves a step closer towards the rational design of nanostructured electrodes. When directly used as an electrode in LIB, this structure exhibited excellent performance in terms of charge-discharge rate, capacity, power density, and cycling stability.

In this study, a thin layer of VOG was grown first on the flat substrate or conformably along the metal foam surfaces. This thin graphene layer promoted vertical growth of NBs into forest structure as well as increased surface roughness of a substrate, enhancing densified nucleation of NBs. It is envisioned that in the future, the substrate, and particularly the metal foam, will be etched off to form freestanding VOG or, in the 3D case, edge oriented graphene (EOG) foam, with significant reduction of the inactive mass of the electrode, similar to the reported smooth graphene foam.^{20,39} However, in contrast to the latter, EOG foam may provide much larger surface area and denser nucleation sites for better active mass loading, and most importantly, it facilitates the orthogonally oriented growth of NBs.

2. Experimental Section

VOG synthesis: VOG was synthesized on flat substrates such as graphite and nickel foil, or 3-D porous substrates such as nickel foams, following the procedure in Ref.⁴⁰ Using a microwave plasma enhanced CVD (PECVD) system. After chemical etching, the substrate placed on a molybdenum sample holder was loaded into the growth chamber, and the chamber was pumped down to 2×10^{-3} torr. At a sample holder temperature of 750 °C, the substrate was further etched by H₂ plasma. Under the condition of CH₄ (50 sccm) and H₂ (100 sccm) gas flow, chamber pressure 30 torr, and 1 kW microwave power, VOG was deposited on the flat substrate or inside Ni foam.

VO₂(B) forest synthesis: VOG sample, V₂O₅ (50 mg) powder, isopropanol (5 ml), and deionized (DI) water (25 ml), were loaded into a Teflon-lined autoclave and maintained at 160-180 °C for up to 48 h in an oven. After synthesis, the sample was washed with DI water and isopropanol several times, and then dried under vacuum at 80 °C for 20 h. The morphology and crystal structure of synthesized VO₂(B) were characterized by scanning electron microscope (SEM), transmission electron microscope (TEM), and X-ray powder diffraction (XRD).

LIB assembling and testing: LIB was assembled in an argon filled glovebox. 3D VO₂(B) NB forest inside Ni foam was directly used as an electrode, with VO₂(B) mass density of 1-2 mg cm⁻², determined by the mass difference before and after VO₂(B) deposition. The electrode, a separator, and a lithium chip were assembled into

a coin cell (CR3032). LiPF_6 (1 M) in EC/DEC/DMC (1:1:1 by volume) was used as electrolyte. A small current of 0.03 mA was employed for first charge-discharge cycle to activate the LIB. Cyclic voltammetry (C-V) measurement of the LIB was carried out over voltage range of 1.5-3.5 V and at different scan rates ranging from 0.1 mV s^{-1} to 2 mV s^{-1} . Charge discharge (C-D) measurements of the LIB were carried out at different current densities varied between 0.1 A g^{-1} and 27 A g^{-1} (0.2 C to 300 C). The cycling life test of the LIB was carried out by performing C-D measurement at a current density of 2 A g^{-1} for 2000 cycles. Electrochemical impedance spectroscopy (EIS) measurement was carried out over frequency range from 1 MHz to 0.1 Hz with 10 mV sine perturbation at 2.5 V.

3. Results and Discussion

3.1. Nanobelt forest on a flat substrate

Figure 1a schematically shows the method to synthesize 2D $\text{VO}_2(\text{B})$ NBs into a forest structure on a flat substrate. A thin layer of VOG, with a vertical thickness of $\sim 1 \mu\text{m}$ is first deposited by PECVD process on a substrate. The growth mechanism of vertically oriented few- or multiple-layer graphene was discussed in many publications.^{41, 42} The SEM images in Figure 1c and Figure S1 of the Supporting Information present examples of the vertically oriented structure of the multilayer graphene (or thin graphite) network. The VOG-coated substrate, loaded with V_2O_5 slurry, is solvothermally treated in an autoclave. Vertically-aligned densely-packed $\text{VO}_2(\text{B})$ NBs are then self-assembled on the VOG-coated substrate into a forest

structure, as illustrated in top view (Figure 1d) and cross-sectional view (Figure 1e) SEM images. The single crystal structure of individual NB can be inferred from the high-resolution TEM image in Figure 1f, that shows a lattice spacing of 0.35 nm, in good agreement with the spacing of the (110) crystal planes of VO₂(B).

Consisting of distorted VO₆ octahedra that share both corners and edges, VO₂(B) has a double-layered V₄O₁₀ crystal structure (Figure 1b), and can form NBs in a solvothermal process, as reported previously.^{35, 37, 38, 43} However, these reported NBs were nucleated homogeneously in the solution to form random clusters. An organized structure, particularly the forest structure reported in this work, is in stark contrast to previous reports. From the microscopic images, here vertically-aligned densely-packed NBs are self-assembled into an ordered nanostructure. Each individual NB has a width of up to 1-2 μm, while its thickness may be as small as a few nanometers. Depending on the synthesis duration, the NB height can go up to tens of micrometers. Such a forest structure with densely-packed VO₂(B) NBs, is a novel structure that has not been explored. A close examination of Figure 1d, e indicates that this structure can probably be better described as 2D NBs-based turf, similar to the artificial green turf (inset of Figure 1e), in contrast to the 1D nanotube- or nanowire-based forest, although we adopt the more common term “forest” to describe this structure.

Figure 2 presents the morphology and crystal structure of one NB forest sample. From the SEM images in Figure 2a-c, careful scrutiny reveals the layered structure of the NBs. Each NB has a variable layer thickness with step ridges along

the growth direction. Although the entire NB assembly is vertically aligned, the top free end of the individual NB forms a curved shape. Owing to the mechanical flexibility of the 2D NBs, the observed bending is probably caused by the surface tension when drying the sample after the solvothermal synthesis. The TEM images shown in Figure 2d, e were acquired for individual NB after peeling off from the substrate using strong ultrasonication. The crystal structure of the NBs was identified using the XRD pattern (Figure 2f), with the XRD peaks indexed to monoclinic VO₂(B) phase based on JCPDS081-2392. No impurity phases were detected. The crystal structure was further confirmed using selected area electron diffraction (SAED). The SAED pattern is shown in the inset of Figure 2e, and confirms the well-defined single-crystal quality. This SAED pattern can be indexed to the [001] zone axis of the monoclinic VO₂(B) phase. The high-resolution TEM image (Figure 2e), taken along the [001] zone axis, reveals a lattice spacing of 0.58 nm, in good agreement with the spacing of the (200) crystal planes of VO₂(B), which produce the XRD peak at 15.3° 2θ (Cu Kα radiation). Therefore, the NB growth is confirmed along the [010] direction.⁴⁴

3.2. Growth mechanism study

Vertically-aligned growth of 2D NBs to form the densely-packed forest structure is novel. To shed light on the growth mechanism present in our synthesis so that similar forest structures can be developed for other layered 2D materials, we varied the VO₂(B) NBs synthesis duration, and the resultant product morphology is

presented in Figure 3. Starting at room temperature and slowly ramping up the autoclave temperature in an oven, after 30 min of solvothermal treatment (Figure 3a), V_2O_5 nanoparticles appeared to be dispersed in the VOG maze and no significant phase transition occurred, as inferred from the particle morphology observations. After 60 min synthesis (Figure 3b), most of the V_2O_5 particles, reduced by isopropanol under the solvothermal high temperature and high pressure conditions, converted into an intermediate phase and coated on the vertical graphene flakes, while some V_2O_5 nanoparticles away from VOG flakes seemed to maintain their particle morphology. After 90 min synthesis (Figure 3c, d), belt-like structures started to form and were vertically oriented. VOG flakes were not clearly discernible, but the maze-like geometry was still observable. This might be due to the complete coverage of VOG flakes by the intermediate phases of vanadium oxide. Belt structures growing along the flakes of VOG maze were observed. After 20-48 h (Figure 3e), the forest structure based on the aligned long NBs was formed on the VOG support. From these observations, a possible growth mechanism of $VO_2(B)$ NB forest is proposed by considering the role of VOG in reference to Figure 3f. It is known that for the VOG, each vertical flake consists of multiple atomic layers with a tapered profile from its thicker bottom to the thinner tip, and therefore a high density of graphene edges exists along the flake wall from the bottom to the top.^{45, 46} These chemically-active unsaturated bonds along graphene step edges provide ideal nucleation sites for NBs^{47, 48}. Accumulation of V_2O_5 and the intermediate phase between and along VOG flakes (Figure 3a, b) may result in a low degree of oversaturation of V^{4+} precursor in the

local solution environment along these fully exposed graphene edges. Therefore, layered VO₂(B) sheets will preferentially nucleate along these active edges to reduce the overall energy, rather than homogeneously in the bulk solution. Then, the belt shape will be formed according to the strong crystal anisotropy of VO₂(B) structure. Vertical walls of VOG might initially guide growth of the nucleated VO₂(B) layered sheets in the vertical direction (Figure 3c, d), and thus serve another purpose in the growth mechanism of VO₂(B) NB forest. The shadowing or crowding effect, due to the densely-packed vertically-aligned NBs, will maintain their vertical growth into a unique forest structure. The critical role of VOG in the forest structure formation was further verified by controlled growth on bare substrates without VOG. These experiments resulted in random NBs precipitation on the substrates, as shown in Figure S2. In addition, our growth also indicated the variation of the NB width that was possibly related to the nucleation rate, kinetically controlled by the slight oversaturation of V⁴⁺ precursor in the local environment of VOG, similar to that observed for other nanosheet growth.⁸ In our solvothermal reactor without solution agitation, the substrate profile variation, leading to the local reactant saturation change, was also found to have influence on the NB growth.

3.3. Forest structure in a 3D conductive foam

From the above growth mechanism, it is expected that in addition to VO₂(B), other layered oxides with demonstrated NB growth in solution, might also nucleate heterogeneously and grow on VOG support into densely-packed forest structures.

Furthermore, in addition to flat substrates, VOG can be conformably coated on any 3D porous substrates that can endure the CVD growth temperature, such as nickel foam. The conformable layer has graphene (or graphite) flakes encircling the nickel skeleton in a radial mode, as shown in Figure 4a-c (and Figure S3a of the Supporting Information), to form edge oriented graphene (EOG) coating. Considering the role of VOG in promoting NB forest growth over a flat substrate, it is not surprising that VO₂(B) NB forest thus can be folded into the EOG-coated nickel foam, and develop a 3D forest structure using a similar solvothermal synthesis process, as schematically illustrated in Figure 4a. Figure 4d, e and Figure S3b of the Supporting Information present the morphology of 3D VO₂(B) NB forest on the EOG-coated foam under different magnifications. The SEM images of interfaces between VO₂(B) NBs and EOG, as well as EOG and Ni foam are shown in Figure S4 of the Supporting Information. These images suggest close interfacial contact that promises a small contact resistance and mechanical strength. Thus, we developed a method to synthesize an ordered macro 3D structure with oriented pores that is based on orthogonally-aligned and densely-packed 2D nanomaterials. Such a structure, with well-connected conductive paths through the underlying foam and a large surface area provided by the 3D NB forest, is well-suited as the electrode architecture for several applications, including LIBs-based energy storage. Freestanding nanostructured electrodes built around nickel foam or graphene foam typically have severe limitations due to the low active mass loading that leaves very large void spacing between skeletons.²⁰ However, for our electrode shown in Figure 4d, the active

VO₂(B) NB forest, with a height larger than 20 μm, occupies almost all spacing inside the compressed foam that has a total thickness of ~ 0.2 mm. Furthermore, similar to the freestanding graphene foam that was formed by etching off nickel foam after CVD growth,^{20, 39} it is expected that in future works, nickel skeleton of our EOG-coated nickel foam can be etched off, leaving only EOG foam as the structure support and current collector, with significant reduction of inactive mass portion in the electrode.

3.4. Electrochemical study for LIB

To demonstrate its utility, a 3D VO₂(B) NB forest grown inside a 3D foam was directly used as an electrode assembled into a coin cell with lithium metal as the other electrode. The geometric area of the electrode was 1.8 cm² and the mass loading of VO₂(B) was 1-2 g cm⁻². All the mass units reported correspond to the VO₂(B) mass. To accurately determine the charge-storage capacity of VO₂(B) forest without the contribution from the underlying foam structure, the capacity of a bare EOG/Ni foam was first tested in a coin cell, and the results are shown in Figure S5 of the Supporting Information. At the lowest current of 0.03 mA investigated, the foam did not contribute to charge storage over a potential range of 1.5-3.0 V (vs. Li/Li⁺). This is because Li⁺-related charge storage in graphite or graphene only occurs at a potential much smaller than 1 V.⁴⁹ Therefore, in the following tests over a potential range of 1.5-3.5 V, we considered the measured capacity exclusively resulted from VO₂(B) material itself. The 3D VO₂(B) NB forest-based cell was activated at a current density

of 0.03 A g^{-1} in the first C-D cycle, as shown in Figure S6 of the Supporting Information. A large charge capacity of 600 mAh g^{-1} and a discharge capacity of 550 mAh g^{-1} were measured. This first C-D cycle exhibited irreversible capacity of 50 mAh g^{-1} with a coulombic efficiency of 92%. In the subsequent test with over 2,000 cycles, the efficiency was maintained at approximately 100%, as will be presented below.

Nanostructured electrodes exhibit large specific capacity and rapid charging-discharging rate capability. The cell was evaluated using C-D measurements at different current densities, and the results are shown in Figure 5. At low current densities, the C-D curves displayed the typical charge and discharge plateaus of $\text{VO}_2(\text{B})$ at approximately 2.5 V (Figure 5a), which corresponds to the $\text{Li}_{0.5}\text{VO}_2$ phase.⁵⁰ The deviation between charge and discharge plateaus increased with the increase of C-D current density. The discharge capacity at a current density of 0.1 A g^{-1} was about 475 mAh g^{-1} . This value is higher than those reported for other $\text{VO}_2(\text{B})$ nanostructures.^{31-33, 35} As shown in Figure 5b, during the first few cycles at low current densities of 0.1 A g^{-1} and 0.2 A g^{-1} , the specific discharge capacity was 475 mAh g^{-1} and 400 mAh g^{-1} , respectively, and the capacity slightly decreased with more cycles used for each current density investigated. A small plateau at approximately 1.7 V on the voltage profiles for the low current densities of 0.1 A g^{-1} and 0.2 A g^{-1} was also observed, similar as that in a previous report.⁵¹ Its source is unclear, but might be related with new phase formation considering that $\text{VO}_2(\text{B})$ is a metastable phase of VO_2 . It is interesting to note that $\text{VO}_2(\text{A})$, another metastable phase of VO_2 ,

also exhibits this plateau at slow discharge rates.⁵² In Figure 5a, this plateau was only observed at a slow discharge process, indicating the phase formation is kinetically controlled. For the current density of 0.5 A g^{-1} after the 12th cycle, the specific capacity was 300 mAh g^{-1} , and subsequently the electrode exhibited constant capacity regardless the number of cycles at any given rate. At a very high current density of 10 A g^{-1} , our $\text{VO}_2(\text{B})$ forest electrode maintained a specific capacity of 178 mAh g^{-1} . This value is much higher than other reports. At the extremely high current density of 27 A g^{-1} , or a rate of 300 C that corresponds to fully charging-discharging in 12 s, our electrode maintained a capacity of 100 mAh g^{-1} .

The many factors that determine the rate capability of an electrode can be modeled into its ohmic resistance R_1 and charge transfer resistance R_2 , in addition to the Warburg impedance W_2 and constant phase element Q_2 related to the interfacial capacitance,⁵³ as shown by the equivalent circuit in the inset of Figure 5c. EIS measurement was conducted, and the resulting Nyquist plot was fitted with R_1 and R_2 being $4.8 \text{ } \Omega$ and $41 \text{ } \Omega$, respectively, for the electrode area of 1.8 cm^2 . These values of ohmic resistance and charge transfer resistance are favorable when compared with the literature values.^{23, 31, 54} These smaller ohmic resistance and charge transfer resistance values indicate good interfacial contact between NBs, EOG, and Ni foam, and further confirm that NB forest electrode promotes the electron and Li^+ ion transportation. The smaller impedance of our electrode results in the observed extraordinary high rate performance.

With the large surface area of the 3D forest structure and the thin 2D NB geometry, the measured storage capacity of the electrode has a significant portion contributed by the surface-related faradaic pseudocapacitance, as well as the storage mechanism of Li^+ intercalation into the bulk of NB lattice. The C-V in Figure 5d displays the typical anodic and cathodic peaks of $\text{VO}_2(\text{B})$ at approximately 2.5 V, which correspond to the formation of Li_xVO_2 .^{31,37} Rather than showing sharp redox peaks, the C-V curves exhibited broad peaks, which indicates the pseudocapacitance effect. This is especially true at the high scan rates of C-V measurements. Following Refs.^{55, 56} the contributions from non-diffusion-limited pseudocapacitance and diffusion-limited intercalation can be obtained by fitting the measured C-V data. Figure 5e shows the fitted contributions from pseudocapacitance and intercalation at different discharge rates. At a discharge rate of 2 C, the contributions from these two mechanisms are roughly the same. It is interesting to note that even at a very low rate of 0.18 C, the capacitance contribution is as high as 20% for such a nanostructured electrode. On the other hand, at high rates, our storage device behaves more like a supercapacitor than a battery. The fading away of the charging-discharging potential plateau in Figure 5a also suggests the dominance of pseudocapacitance effect at a high rate.

A noteworthy feature of the NB forest-based electrode is the good cycling stability even at a high current density. As shown in Figure 5f, after C-D test for 5 cycles at each high current density varied from 1 A g^{-1} to 27 A g^{-1} , 100% of the original capacity was recovered when cycling test returned to 0.5 A g^{-1} . Subsequently,

this same cell was further measured for 2,000 cycles at a high current density of 2 A g⁻¹. As shown in Figure 5f, the capacity of the electrode at 2 A g⁻¹ maintained 90% of its initial value after 1,000 cycles, and 79% after 2,000 cycles. Meanwhile, the coulombic efficiency, even at 2 A g⁻¹, remained at close to 100% over 2,000 cycles. The demonstrated stability of our electrode based on VO₂(B) NB forest is much better than other VO₂(B) nanostructured electrodes reported in the literatures,^{31, 33, 35, 50} although further improvement is still necessary. The much better cycling performance of our VO₂(B) NB forest based electrode demonstrates the superiority of this freestanding electrode architecture. Such a freestanding electrode, with VO₂(B) NBs directly nucleate and grow inside the EOG/Ni foam without using any polymer binders and conductive fillers, ensures the electrode integrity. The thin NBs relieve the generated lattice strain during lithiation/delithiation, while the space between neighboring NBs can buffer the crystal volume expansion. These will further minimize the possibility of electrode pulverization. However, we did observe a relatively sharp decrease of the capacity in the first 300 cycles. This might be caused by some NBs that had a weakened connection with EOG/Ni foam caused by the applied mechanical force during the cell assembling.

4. Conclusions

In summary, vertically-aligned and densely-packed forest structure based on VO₂(B) NB forest is reported. The structure was synthesized with VOG as a support using solvothermal method. This forest structure was further folded into conductive

Ni foam to construct a 3D ordered macrostructure that was directly applied as an electrode for LIBs. The tens of micrometer scale height of NB forest ensures the filling of active mass into the void spacing of the conductive foam. It is also expected that by etching off the Ni foam, edge oriented graphene foam can act as both the structure scaffold and the current collector to minimize the inactive mass ratio of the whole electrode. The battery performance test confirmed that such a 3D ordered structure based on 2D nanomaterial exhibits excellent performance in terms of charging-discharging rate, capacity, and cycling stability. It is expected that our approach, which utilizes VOG or 3D EOG as support to synthesize VO₂(B) NB forest structures, can be extended to a variety of other layered oxide and hydroxide materials, exploring their 2D properties in a unique 3D forest structure for energy conversion, storage, and other applications.

Supporting Information

Additional SEM images of different microstructures and other battery test data are available in the Supporting Information.

References

1. F. Bonaccorso, L. Colombo, G. Yu, M. Stoller, V. Tozzini, A. C. Ferrari, R. S. Ruoff and V. Pellegrini, *Science*, 2015, **347**, 41.
2. S. Z. Butler, S. M. Hollen, L. Cao, Y. Cui, J. A. Gupta, H. R. Gutierrez, T. F. Heinz, S. S. Hong, J. Huang and A. F. Ismach, *ACS nano*, 2013, **7**, 2898-2926.
3. X. Peng, L. Peng, C. Wu and Y. Xie, *Chem. Soc. Rev.*, 2014, **43**, 3303-3323.
4. C. Yuan, J. Li, L. Hou, X. Zhang, L. Shen and X. W. D. Lou, *Adv. Func. Mater.*, 2012, **22**, 4592-4597.

5. J. Cheng, B. Wang, H. L. Xin, G. Yang, H. Cai, F. Nie and H. Huang, *J. Mater. Chem. A*, 2013, **1**, 10814-10820.
6. L. Peng, X. Peng, B. Liu, C. Wu, Y. Xie and G. Yu, *Nano Lett.*, 2013, **13**, 2151-2157.
7. E. Hosono, S. Fujihara, I. Honma and H. Zhou, *Adv. Mater.*, 2005, **17**, 2091-2094.
8. E. Hosono, H. Matsuda, I. Honma, M. Ichihara and H. Zhou, *Langmuir*, 2007, **23**, 7447-7450.
9. X. W. D. Lou, *Energy Environ. Sci*, 2012, **5**, 7883-7887.
10. G. Zhang and X. W. D. Lou, *Adv. Mater.*, 2013, **25**, 976-979.
11. H. Chen, L. Hu, M. Chen, Y. Yan and L. Wu, *Adv. Func. Mater.*, 2014, **24**, 934-942.
12. H. Zhong, G. Yang, H. Song, Q. Liao, H. Cui, P. Shen and C.-X. Wang, *J. Phys. Chem. C*, 2012, **116**, 9319-9326.
13. H. Zhang, X. Yu and P. V. Braun, *Nat. nanotechnol.*, 2011, **6**, 277-281.
14. B. L. Ellis, P. Knauth and T. Djenizian, *Adv. Mater.*, 2014, **26**, 3368-3397.
15. S. Chabi, C. Peng, D. Hu and Y. Zhu, *Adv. Mater.*, 2014, **26**, 2440-2445.
16. X. Zhang, I. Belharouak, L. Li, Y. Lei, J. W. Elam, A. Nie, X. Chen, R. S. Yassar and R. L. Axelbaum, *Adv. Energy Mater.*, 2013, **3**, 1299-1307.
17. P. Xiong, L. Peng, D. Chen, Y. Zhao, X. Wang and G. Yu, *Nano Energy*, 2015, **12**, 816-823.
18. C. Wu, X. Lu, L. Peng, K. Xu, X. Peng, J. Huang, G. Yu and Y. Xie, *Nat. Commun.*, 2013, **4**.
19. G.-W. Yang, C.-L. Xu and H.-L. Li, *Chem. Commun.*, 2008, 6537-6539.
20. D. Chao, X. Xia, J. Liu, Z. Fan, C. F. Ng, J. Lin, H. Zhang, Z. X. Shen and H. J. Fan, *Adv. Mater.*, 2014, **26**, 5794-5800.
21. G. Q. Zhang, H. B. Wu, H. E. Hoster, M. B. Chan-Park and X. W. D. Lou, *Energy Environ. Sci*, 2012, **5**, 9453-9456.
22. D. Chao, C. Zhu, X. Xia, J. Liu, X. Zhang, J. Wang, P. Liang, J. Lin, H. Zhang, Z. Shen and H. J. Fan, *Nano Lett.*, 2015, **15**, 565.
23. X. Huang, H. Yu, J. Chen, Z. Lu, R. Yazami and H. H. Hng, *Adv. Mater.*, 2014.
24. S. A. Klankowski, R. A. Rojas, B. A. Cruden, J. Liu, J. Wu and J. Li, *J. Mater. Chem. A*, 2013, **1**, 1055-1064.
25. C. Cheng, B. Liu, H. Yang, W. Zhou, L. Sun, R. Chen, S. F. Yu, J. Zhang, H. Gong and H. Sun, *ACS Nano*, 2009, **3**, 3069-3076.
26. C. Zhu, X. Xia, J. Liu, Z. Fan, D. Chao, H. Zhang and H. J. Fan, *Nano Energy*, 2014, **4**, 105-112.
27. C. Nethravathi, C. R. Rajamathi, M. Rajamathi, U. K. Gautam, X. Wang, D. Golberg and Y. Bando, *ACS Appl. Mater. Interfaces*, 2013, **5**, 2708-2714.
28. L. Mai, Q. An, Q. Wei, J. Fei, P. Zhang, X. Xu, Y. Zhao, M. Yan, W. Wen and L. Xu, *Small*, 2014, **10**, 3032-3037.
29. Y. Tang, H. Cong, F. Li and H.-M. Cheng, *Diam. Relat. Mater.*, 2007, **16**, 537-541.

30. Y. Wei, Y. Ding, C. Li, S. Xu, J.-H. Ryo, R. Dupuis, A. K. Sood, D. L. Polla and Z. L. Wang, *J. Phys. Chem. C*, 2008, **112**, 18935-18937.
31. L. Mai, Q. Wei, Q. An, X. Tian, Y. Zhao, X. Xu, L. Xu, L. Chang and Q. Zhang, *Adv. Mater.*, 2013, **25**, 2969-2973.
32. H. Liu, Y. Wang, K. Wang, E. Hosono and H. Zhou, *J. Mater. Chem.*, 2009, **19**, 2835-2840.
33. C. J. Niu, J. S. Meng, C. H. Han, K. N. Zhao, M. Y. Yan and L. Q. Mai, *Nano Lett.*, 2014, **14**, 2873-2878.
34. A. Pan, H. B. Wu, L. Yu and X. W. D. Lou, *Angew. Chem. Int. Ed.*, 2013, **125**, 2282-2286.
35. Q. Zhao, L. Jiao, W. Peng, H. Gao, J. Yang, Q. Wang, H. Du, L. Li, Z. Qi and Y. Si, *J. Power Sources*, 2012, **199**, 350-354.
36. M. Rahman, J.-Z. Wang, N. H. Idris, Z. Chen and H. Liu, *Electrochim. Acta*, 2010, **56**, 693-699.
37. S. Yang, Y. Gong, Z. Liu, L. Zhan, D. P. Hashim, L. Ma, R. Vajtai and P. M. Ajayan, *Nano Lett.*, 2013, **13**, 1596-1601.
38. K.-F. Zhang, S.-J. Bao, X. Liu, J. Shi, Z.-X. Su and H.-L. Li, *Mate. Res. Bull.*, 2006, **41**, 1985-1989.
39. X. Xiao, P. Liu, J. S. Wang, M. Verbrugge and M. P. Balogh, *Electrochem. Commun.*, 2011, **13**, 209-212.
40. G. Ren, X. Pan, S. Bayne and Z. Fan, *Carbon*, 2014.
41. A. Malesevic, R. Vitchev, K. Schouteden, A. Volodin, L. Zhang, G. Van Tendeloo, A. Vanhulsel and C. Van Haesendonck, *Nanotechnology.*, 2008, **19**, 305604.
42. M. Cai, R. A. Outlaw, S. M. Butler and J. R. Miller, *Carbon*, 2012, **50**, 5481-5488.
43. C. Wu, F. Feng and Y. Xie, *Chem. Soc. Rev.*, 2013, **42**, 5157-5183.
44. M. Li, F. Kong, Y. Zhang and G. Li, *CrystEngComm*, 2011, **13**, 2204-2207.
45. X. Pan, K. Zhu, G. Ren, N. Islam, J. Warzywoda and Z. Fan, *J. Mater. Chem. A*, 2014.
46. J. Zhao, M. Shaygan, J. R. Eckert, M. Meyyappan and M. H. Rummeli, *Nano Lett.*, 2014, **14**, 3064-3071.
47. K. Kim, R. W. Johnson, J. T. Tanskanen, N. Liu, M.-G. Kim, C. Pang, C. Ahn, S. F. Bent and Z. Bao, *Nat. Commun.*, 2014, **5**.
48. H.-B.-R. Lee, S. H. Baeck, T. F. Jaramillo and S. F. Bent, *Nano Lett.*, 2013, **13**, 457-463.
49. E. Yoo, J. Kim, E. Hosono, H.-S. Zhou, T. Kudo and I. Honma, *Nano Lett.*, 2008, **8**, 2277-2282.
50. B. Zachau-Christiansen, K. West and T. Jacobsen, *Mater. Res. Bull.*, 1985, **20**, 485-492.
51. C. Nethravathi, B. Viswanath, J. Michael and M. Rajamath, *Carbon*, 2012, **50**, 4839-4846.
52. L. Dai, Y. Gao, C. Cao, Z. Chen, H. Luo, M. Kanehira, J. Jin and Y. Liu, *RSC Adv.*, 2012, **2**, 5265-5270.

53. C. Lin, B. Ding, Y. Xin, F. Cheng, M. O. Lai, L. Lu and H. Zhou, *J. Power Sources*, 2014, **248**, 1034-1041.
54. D. Wang, D. Choi, J. Li, Z. Yang, Z. Nie, R. Kou, D. Hu, C. Wang, L. V. Saraf and J. Zhang, *ACS nano*, 2009, **3**, 907-914.
55. M. Sathiya, A. Prakash, K. Ramesha, J. M. Tarascon and A. Shukla, *J. Am. Chem. Soc.*, 2011, **133**, 16291-16299.
56. K. Zhu, Q. Wang, J.-H. Kim, A. A. Pesaran and A. J. Frank, *J. Phy. Chem. C*, 2012, **116**, 11895-11899.

Figure Captions

Figure 1. (a) Schematic shows the VO₂(B) NB-based forest structure being synthesized on a VOG-coated flat substrate. (b) Lattice structure illustrates the double-layered crystal structure of VO₂(B). Crystal directions a, b, c represent [100], [010], [001] directions, respectively. (c) Cross-sectional SEM image of VOG. (d, e) SEM images of one representative VO₂(B) NB forest with the width of an individual NB of 1-2 μm. The inset of (e) depicts a photo picture of artificial turf for comparison. (f) High-resolution TEM image indicates a single-crystal structure of an individual NB. The lattice spacing of 0.35 nm corresponds to the (110) crystal plane of VO₂(B).

Figure 2. (a-c) SEM images of VO₂(B) NB forest at several different magnifications. (d) TEM image of an individual NB. (e) High-resolution TEM image taken along the [001] zone axis shows the (200) crystal plane, indicating the NB growth along the [010] direction. The SAED pattern (inset) taken along the [001] zone axis further confirms the single-crystal quality. (f) XRD pattern (Cu Kα radiation) can be indexed to the monoclinic VO₂(B) phase based on JCPDS081-2392. The three intense peaks, marked “Al” are from the aluminum sample holder used in XRD analysis.

Figure 3. (a-e) SEM images showing the NB forest growth mechanism. (a) V₂O₅ nanoparticles dispersed in the VOG network. (b) Intermediate phase of vanadium oxide precursor dispersed on VOG walls, captured at a time when VO₂(B) phase started to nucleate. (c, d) VO₂(B) NBs nucleated along the exposed graphene edges

and grew out of the VOG network in the vertical orientation. (e) VO₂(B) NB forest grew out of VOG after 20-48 h solvothermal process. (f) TEM image of VOG flake and schematic (inset) indicate flake's multiple atomic layers with a tapered profile from its thicker bottom to the thinner tip with fully exposed step edges.

Figure 4. (a) Schematic of 3D VO₂(B) NB forest synthesis shows that the EOG structure is first grown around the Ni foam skeleton, and then, using EOG/Ni foam as a support, 3D VO₂(B) NB forest structure is synthesized inside the foam. (b, c) SEM images of EOG/Ni foam. The inset of (c) is the TEM image of EOG flake. (d, e) SEM images of 3D VO₂(B) NB forest. The inset of (d) is the cross-sectional view SEM image of VO₂(B) NB forest in EOG/Ni foam that indicates most space in the foam is occupied by VO₂(B) active material. The top inset of (e) is the TEM image of an individual NB, and the bottom inset of (e) is the cross-sectional view SEM image of NB forest.

Figure 5. Experimental results for the LIB based on 3-D VO₂(B) NB forest, which was used as an electrode. (a) C-D curves at different current densities. (b) Rate performance and cycling performance. (c) Nyquist plot of the LIB impedance. (d) C-V curve at a scan rate of 0.1 mV s⁻¹. (e) Contribution of non-diffusion-limited pseudocapacitance and diffusion-limited intercalation to the total capacity at different discharge current densities. (f) Cycling stability and Coulombic efficiency tested at a current density of 2A g⁻¹ over 2000 cycles.

Figure 1

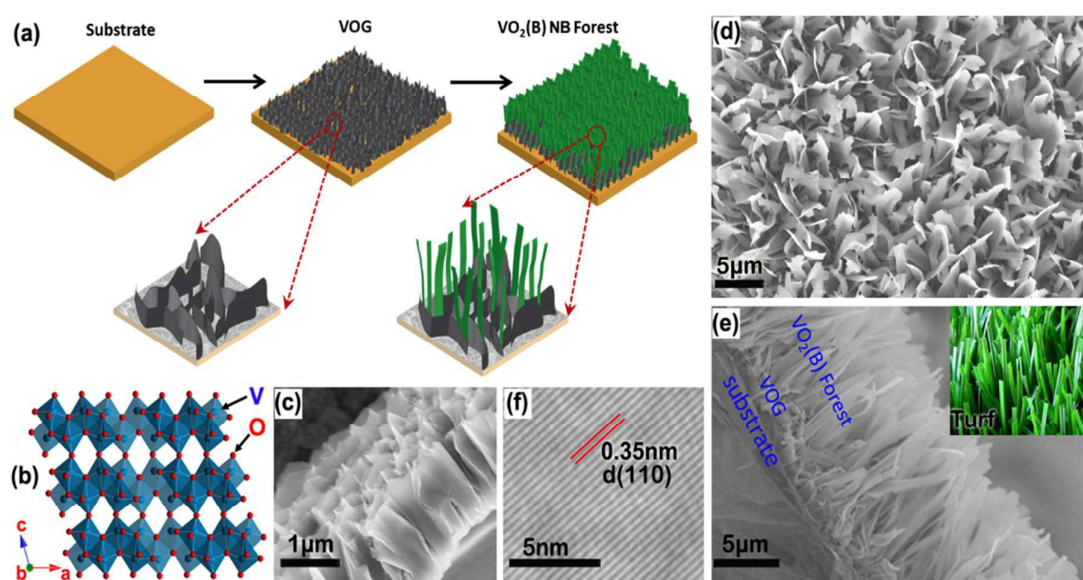


Figure 2

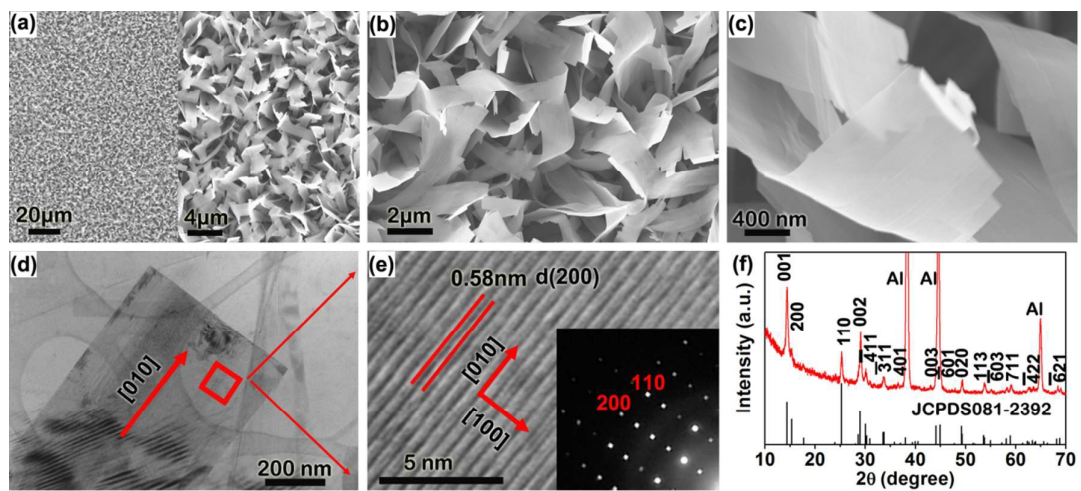


Figure 3

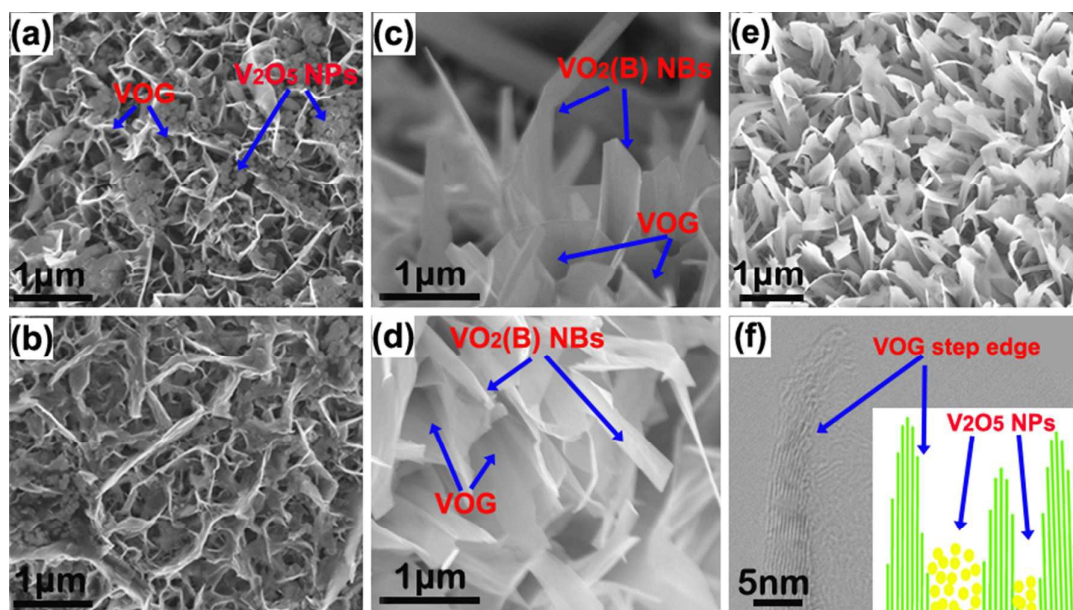


Figure 4

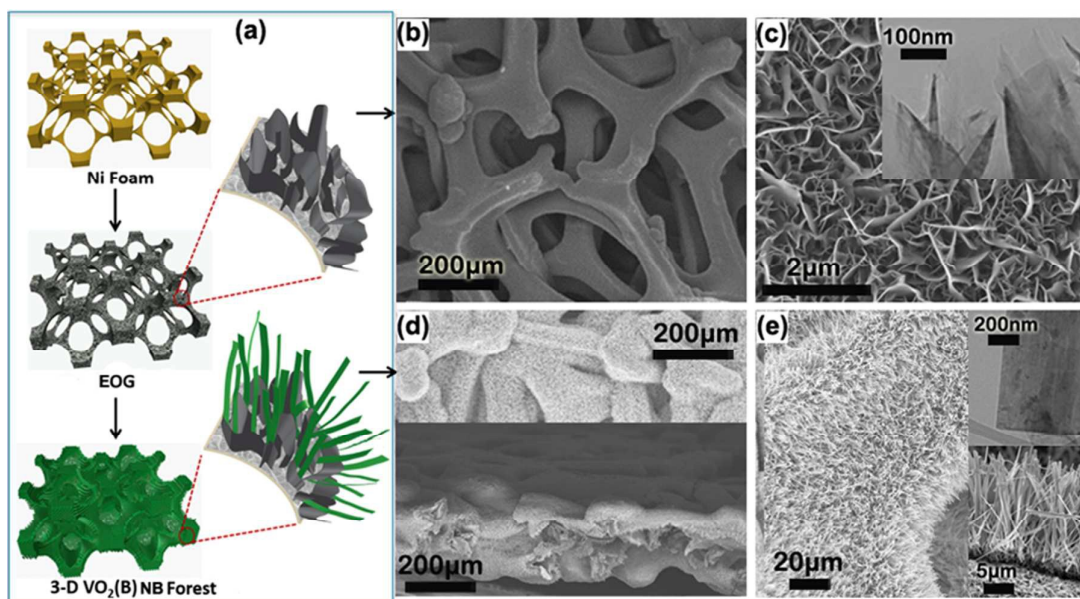
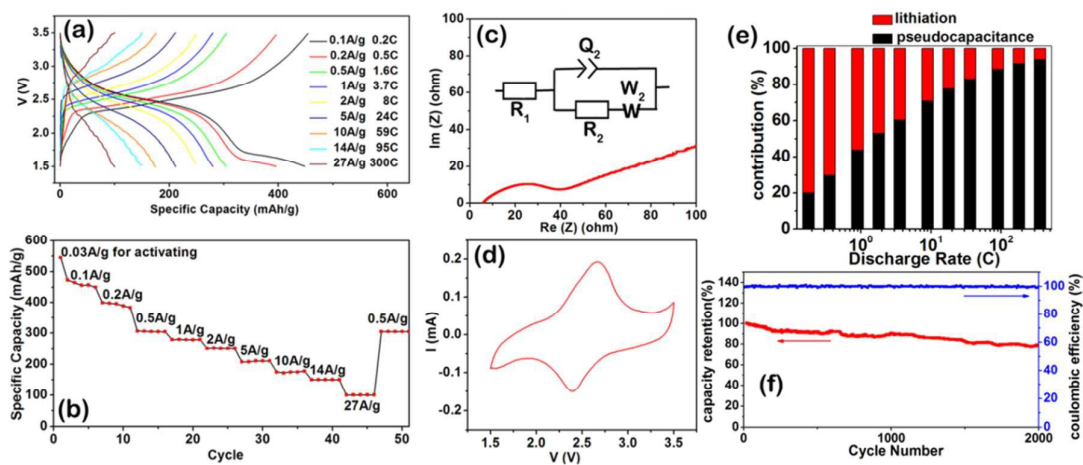
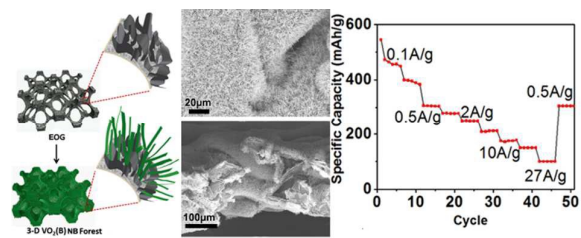


Figure 5



TOC



Assembling two-dimensional graphene and VO₂(B) nanomaterials into an ordered three-dimensional forest structure for high performance lithium ion batteries